

Article

Effect of Ta and W Additions on Microstructure and Mechanical Properties of Tilt-Cast Ti-45Al-5Nb-2C Alloy

Juraj Lapin *  and Kateryna Kamyshnykova

Institute of Materials and Machine Mechanics, Slovak Academy of Sciences, Dúbravská cesta 9, 845 13 Bratislava, Slovakia; kateryna.kamyshnykova@savba.sk

* Correspondence: juraj.lapin@savba.sk

Abstract: The effect of Ta and W additions on microstructure and mechanical properties of tilt-cast Ti-45Al-5Nb-2C (at.%) alloy was investigated. Three alloys with nominal composition Ti-45Al-5Nb-2C-2X (in at.%), where X is Ta or W, were prepared by vacuum induction melting in graphite crucibles followed by tilt casting into graphite moulds. The microstructure of the tilt-cast alloys consists of the $\alpha_2(\text{Ti}_3\text{Al}) + \gamma(\text{TiAl})$ lamellar grains, single γ phase, $(\text{Ti,Nb,X})_2\text{AlC}$ particles with a small amount of $(\text{Ti,Nb,X})\text{C}$, and $\beta/\text{B2}$ phase identified only in W containing alloy. The EDS analysis shows that Ta segregates into the carbide particles and reduces dissolution of Nb in both $(\text{Ti,Nb,Ta})\text{C}$ and $(\text{Ti,Nb,Ta})_2\text{AlC}$ phases. The alloying with W reduces Nb content in both carbide phases and leads to stabilisation of $\beta/\text{B2}$ phase in the lamellar $\alpha_2 + \gamma$ regions. The alloying with Ta and W does not affect the volume fraction of the carbide particles but influences their size and morphology. While the alloying with Ta and W has no significant effect on Vickers hardness and the indentation elastic modulus of the studied alloys, the addition of Ta affects the nanohardness and elastic modulus of the $(\text{Ti,Nb,Ta})_2\text{AlC}$ phase. The addition of W significantly increases the Vickers microhardness of the lamellar $\alpha_2 + \gamma$ regions.



Citation: Lapin, J.; Kamyshnykova, K. Effect of Ta and W Additions on Microstructure and Mechanical Properties of Tilt-Cast Ti-45Al-5Nb-2C Alloy. *Metals* **2021**, *11*, 2052. <https://doi.org/10.3390/met11122052>

Academic Editor:
Wojciech Szkliniarz

Received: 22 November 2021
Accepted: 14 December 2021
Published: 18 December 2021

Publisher's Note: MDPI stays neutral with regard to jurisdictional claims in published maps and institutional affiliations.



Copyright: © 2021 by the authors. Licensee MDPI, Basel, Switzerland. This article is an open access article distributed under the terms and conditions of the Creative Commons Attribution (CC BY) license (<https://creativecommons.org/licenses/by/4.0/>).

Keywords: intermetallics; TiAl; induction melting; casting; carbides; graphite crucibles; microstructure; mechanical properties

1. Introduction

Lightweight alloys based on a TiAl-Nb system are of great interest for applications in aerospace, power engineering, and automotive industry due to their high melting point, low density, high specific strength, and good creep and oxidation resistance [1–5]. Nb is a common alloying element in numerous TiAl-based alloys with high solubility and different partition between $\gamma(\text{TiAl})$ and $\alpha_2(\text{Ti}_3\text{Al})$ phases as well as different influences on the lattice parameters of both phases [6]. The effects of Nb on the microstructure, creep properties, oxidation resistance, and deformation mechanisms of TiAl-based alloys have been well studied [7–11]. Further expansion of the usability of TiAl-Nb alloys can be achieved by improving their properties through additional alloying elements such as Ta, W, and C.

Ta, as the slower diffuser than Nb in TiAl-based alloys, is considered to be the most effective solute atom to promote the formation of massive $\gamma_m(\text{TiAl})$ phase in air-cooling conditions that have a great opportunity to improve the properties of TiAl-Ta alloys [12,13]. Zhang et al. [14,15] have reported that the addition of 0.5–1 at.% Ta promotes the formation of ultrafine $\gamma(\text{TiAl})$ grains through the formation of massive γ_m phase during quenching from α (Ti-based solid solution with a hexagonal crystal structure) phase field and leads to an improvement of mechanical properties. Vojtěch et al. [16,17] have shown that the addition of Ta to TiAl improves both creep strength and high-temperature cyclic oxidation resistance compared to those of TiAl-Nb alloy. Lapin et al. [18,19] have reported that Ta retards the transformation of α_2 lamellae to γ phase and $\tau(\text{Ti}_3\text{Al}_2\text{Ta})$ precipitates and stabilises the lamellar $\alpha_2 + \gamma + \tau$ type of microstructure of TiAl-Ta alloy during long-term ageing at 750 °C up to 10,000 h or creep exposure at 700 °C up to 30,000 h.

The positive effect of W addition on mechanical properties of TiAl-W alloys has been attributed to a reduction in the dislocation mobility and pinning of lamellar $\alpha_2 + \gamma$ interfaces by fine B2 (ordered Ti-based solid solution with a cubic crystal structure) precipitates [20]. The high capability of W to significantly improve creep resistance of TiAl-W alloys has been demonstrated by Beddoes et al. [20–22], Couret et al. [23], and Lapin and Nazmy [24–26]. However, a significant softening has been observed at temperatures of 900–1000 °C due to instability of the lamellar $\alpha_2 + \gamma$ microstructure [27,28].

Alloying with C below its solubility limit contributes to the solid solution hardening of TiAl-Nb alloys. As shown for several TiAl-based alloys [29–32], cubic perovskite needle-like Ti_3AlC carbide particles, which are thermodynamically stable at medium temperatures, enhance strength and creep resistance due to precipitation hardening. On the contrary, fine hexagonal plate-like Ti_2AlC carbide particles, which are thermodynamically stable at higher temperatures, are less efficient to impede dislocation mobility [33–35]. It has been reported that the alloying with C above its solubility affects the solidification path, changes the primary solidification phase, and leads to the formation of coarse primary Ti_2AlC particles during solidification of TiAl-Nb alloys [32,36–42].

Various methods such as powder metallurgy, mechanical alloying, vacuum induction melting, etc., were applied for the processing of TiAl-based alloys. Among them, vacuum induction melting (VIM) combined with precise casting is identified to be one of the most cost-effective processing routes for the production of near net shape components. Several ceramic materials have been evaluated for melting and casting of TiAl-based alloys but none of them were inert against their melts. VIM in relatively cheap graphite crucibles and casting into graphite moulds represents a cost-effective way for processing TiAl-based castings. This process leads to an increase in C in TiAl-based alloys. However, the content of C can be controlled by an appropriate selection and optimisation of processing parameters, such as heating rate, melt temperature, holding time at the melt temperature, arrangement of the charge in a graphite crucible, chemical composition of master alloys, and vacuum pressure [43–48].

Despite previous studies on microstructure and mechanical properties of carbon-containing TiAl-Nb alloys reinforced with coarse primary Ti_2AlC particles [39,49–51], only very limited information has been published about the effect of Ta and W on their microstructure, solidification behaviour, and properties [52]. This study aims to investigate the effect of Ta and W additions on the tilt-cast microstructure and room temperature mechanical properties of Ti-45Al-5Nb-2C (at.%) alloy. The effect of alloying with Ta and W on the chemical composition of coexisting phases, solidification behaviour, elastic modulus, hardness, microhardness, and nanohardness is investigated and discussed.

2. Materials and Methods

Three alloys with nominal compositions Ti-45Al-5Nb-2C-2X (at.%), where X is Ta or W, were prepared from a master alloy with nominal composition Ti-43.5Al-1Nb (at.%). The cylindrical pieces of the master alloy with a diameter of 60 mm and height of 15 mm were mixed with additions of pure elements in the form: sponge of Ti, rectangular pieces of Al, Nb sheet, Ta chips, W powder, and TiC powder. The charge with a weight of 490 g was placed into a graphite crucible with an inner diameter of 65 mm and a length of 135 mm. The graphite crucible was put into a protective alumina-based crucible equipped with a pouring cup, which was connected to a cylindrical graphite mould with an inner diameter of 40 mm and length of 230 mm. Before the heating, the vacuum chamber of the induction melting furnace was evacuated to a vacuum pressure of 6.5 Pa and flushed with argon (purity 99.9995%) three times. After increasing the vacuum pressure to 1×10^4 Pa by a partial filling of the vacuum chamber with high purity argon, the charge was heated to a melt temperature of 1650 °C and held at this temperature for 30 s. The temperature of the melt was measured by a pyrometer. The tilt casting was carried out into a cold graphite mould under the vacuum pressure corresponding to that of VIM. The tranquil filling of the mould with minimum surface turbulence was achieved by a control

of the tilting speed. The cylindrical tilt-cast samples were cut transversally into smaller pieces for metallographic observations and mechanical testing using an electric spark wire cutting machine.

Metallographic preparation of the samples consisted of standard grinding using abrasive papers, polishing on diamond pastes with various grain sizes up to 0.25 μm , and etching in a solution of 100 mL H_2O , 6 mL HNO_3 , and 3 mL HF. Microstructure evaluation was performed by scanning electron microscopy (SEM) and scanning electron microscopy in back-scattered electron (BSE) mode using JEOL 7600F field emission scanning electron microscope. The X-ray diffraction (XRD) analysis of coexisting phases was carried out by a diffractometer Bruker D8 equipped with an X-ray tube with a rotating Cu anode operating at 12 kW. The chemical composition of the alloys was analysed by energy-dispersive spectrometry (EDS) calibrated using the standards (TiC, TaC, and Ti_2AlC) for measurements of the composition of carbides. The average content of carbon in the tilt-cast alloys was measured by LECO CS844 elemental analyser. The average contents of oxygen and nitrogen were measured by a LECO ONH836 elemental analyser. Grain size, interlamellar spacing, volume fraction, and size of particles were measured by computerised image analysis using digitalised micrographs. The measured microstructural data were treated statistically.

Instrumented hardness measurements were performed by a universal testing machine. Instrumented Martens hardness measurements were carried out at an applied load of 298 N, holding time at the point of load application of 0.1 s, and rate of load application of 15 N/s. Vickers hardness measurements were performed at an applied load of 298 N and holding time at the point of load application of 10 s. Vickers microhardness measurements were carried out at an applied load of 0.49 N and a dwell time of 10 s on polished and slightly etched sections of the tilt-cast samples. Instrumented nanoindentation measurements were carried out at an applied load of 0.01 N and holding time at the point of load application of 0.1 s on polished and slightly etched samples using a nanoindenter with Berkovich tip of the indenter.

3. Results

3.1. Chemical Composition

Table 1 summarises nominal and measured chemical compositions with standard errors of the measurements of the studied tilt-cast alloys. It is clear from Table 1 that the measured average contents of the alloying elements in the tilt-cast alloys designated as Nb, NbTa, and NbW correspond well to their designed nominal compositions. In addition, the applied cost-effective processing route consisting of VIM in graphite crucibles followed by tilt casting into cold graphite moulds leads to an acceptable increase in gases significantly affecting solidification behaviour [53–56]. The initial contents of oxygen and nitrogen of 510 and 170 wt.ppm measured in the charge increased up to 870 and 235 wt.ppm in the tilt-cast Nb, NbTa, and NbW alloys, respectively. The present results indicate that VIM in graphite crucibles followed by casting into graphite moulds can be applied for processing of TiAl-based alloys containing minor additions of strong carbide forming elements such as Nb, Ta, and W.

Table 1. Nominal and measured chemical composition of studied tilt-cast alloys (at.%).

Alloy		Ti	Al	Nb	Ta	W	C
Nb	nominal	48	45	5	-	-	2
	measured	48.1 ± 0.3	44.9 ± 0.3	5.0 ± 0.1	-	-	2.0 ± 0.1
NbTa	nominal	46	45	5	2	-	2
	measured	46.2 ± 0.2	44.9 ± 0.2	5.0 ± 0.1	2.0 ± 0.1	-	1.9 ± 0.1
NbW	nominal	46	45	5	-	2	2
	measured	46.0 ± 0.3	45.0 ± 0.3	5.1 ± 0.1	-	2.0 ± 0.1	2.1 ± 0.1

3.2. Microstructure and Phase Analysis

Figure 1 shows the typical microstructures of the tilt-cast Nb, NbTa, and NbW alloys. The microstructure of the alloys consists of the matrix composed of two single phases (1 and 5) and lamellar regions (2). The matrices of the alloys are reinforced with relatively uniformly distributed plate-like and irregularly shaped particles (3 and 4), as seen in Figure 1a,c and e. Figure 2 shows XRD diffraction patterns and summarises four identified coexisting phases in the studied alloys: α_2 , γ , β /B2, and Ti_2AlC . Table 2 shows the average chemical composition with standard error of the measurement of the coexisting phases and microstructural regions measured by EDS. Based on the measured chemical composition and XRD analyses, the microstructure of the studied Nb, NbTa, and NbW alloys consist of equiaxed $\alpha_2 + \gamma$ lamellar grains and grain boundaries containing a single γ phase, as seen in Figure 1b,d and f. In addition, the matrix of the NbW alloy contains an irregular network enriched in Nb and W that belongs to β /B2 phase (disordered/ordered Ti-based solid solution with a cubic crystal structure), as seen in Figure 1f and Table 2. Figures 3–5 show the distribution of alloying elements in the reinforcing carbide particles and the surrounding matrix. In all studied alloys, cores of the coarse irregular shaped $(\text{Ti,Nb,X})_2\text{AlC}$ particles, where X is Ta or Nb, are enriched in Ti but depleted in Al and Nb compared to those of the surrounding $(\text{Ti,Nb,X})_2\text{AlC}$ phase or the matrix. The measured chemical compositions of these particles correspond to the $(\text{Ti,Nb,X})\text{C}$ phase but their amount in the studied Nb, NbTa, and NbW alloys are under the detectable limit of the XRD analysis. The EDS map and point analyses indicate that Ta as a strong carbide forming element segregates intensively to both carbide phases in the NbTa alloy, as seen in Figure 4 and Table 2. However, its content is slightly higher in $(\text{Ti,Nb,Ta})\text{C}$ than in $(\text{Ti,Nb,Ta})_2\text{AlC}$. Alloying with Ta reduces the dissolution of Nb in both $(\text{Ti,Nb,Ta})\text{C}$ and $(\text{Ti,Nb,Ta})_2\text{AlC}$ phases compared to that in the Nb alloy. The EDS maps in Figure 5 and Table 2 indicate that W in the NbW alloy segregates predominantly to the β /B2 phase and its dissolution is reduced in $(\text{Ti,Nb,W})\text{C}$ and $(\text{Ti,Nb,W})_2\text{AlC}$ phases. Alloying with W leads to a decrease in Nb content in both $(\text{Ti,Nb,W})\text{C}$ and $(\text{Ti,Nb,W})_2\text{AlC}$ phases and increases its content in the lamellar $\alpha_2 + \gamma$ regions compared to those in the Nb alloy, as shown in Table 2.

Table 2. Chemical composition of coexisting phases of the studied alloys (at.%).

Alloy	Region	Phase	Ti	Al	Nb	Ta	W	C
Nb	1	γ	46.8 ± 0.2	48.1 ± 0.2	5.1 ± 0.1	-	-	-
	2	$\alpha_2 + \gamma$	48.5 ± 0.1	45.8 ± 0.2	5.7 ± 0.1	-	-	-
	3	TiC	55.6 ± 0.8	1.5 ± 0.4	2.8 ± 0.2	-	-	40.1 ± 0.7
	4	Ti_2AlC	44.2 ± 0.2	24.6 ± 0.1	4.3 ± 0.1	-	-	26.9 ± 0.4
NbTa	1	γ	45.9 ± 0.2	47.6 ± 0.3	5.4 ± 0.1	1.1 ± 0.1	-	-
	2	$\alpha_2 + \gamma$	46.7 ± 0.1	46.3 ± 0.2	5.8 ± 0.1	1.2 ± 0.1	-	-
	3	TiC	44.4 ± 0.1	0.4 ± 0.2	3.1 ± 0.1	5.8 ± 0.1	-	46.3 ± 0.5
	4	Ti_2AlC	42.0 ± 0.3	23.6 ± 0.4	3.8 ± 0.1	3.9 ± 0.1	-	26.7 ± 0.5
NbW	1	γ	43.6 ± 0.2	50.5 ± 0.3	5.0 ± 0.2	-	0.9 ± 0.1	-
	2	$\alpha_2 + \gamma$	45.3 ± 0.1	47.1 ± 0.2	6.2 ± 0.1	-	1.4 ± 0.1	-
	3	TiC	53.9 ± 0.9	2.1 ± 0.9	2.1 ± 0.4	-	0.2 ± 0.1	41.7 ± 0.4
	4	Ti_2AlC	45.2 ± 0.9	23.7 ± 1.2	3.6 ± 0.2	-	0.4 ± 0.1	27.1 ± 0.6
	5	β	46.8 ± 0.1	38.6 ± 0.2	8.2 ± 0.1	-	6.4 ± 0.1	-

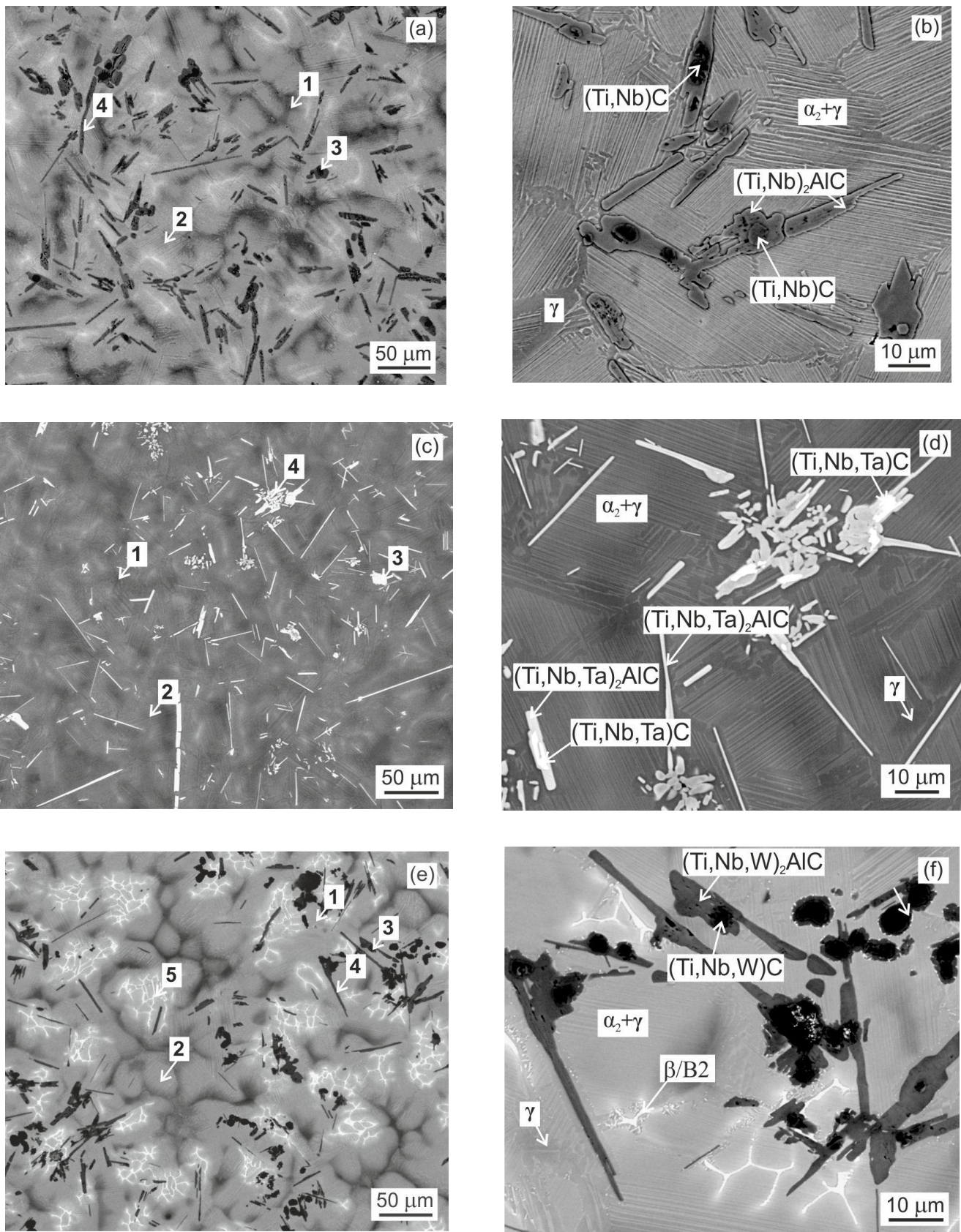


Figure 1. BSE micrographs showing the microstructure of tilt-cast alloys: (a,b) Nb, (c,d) NbTa, and (e,f) NbW.

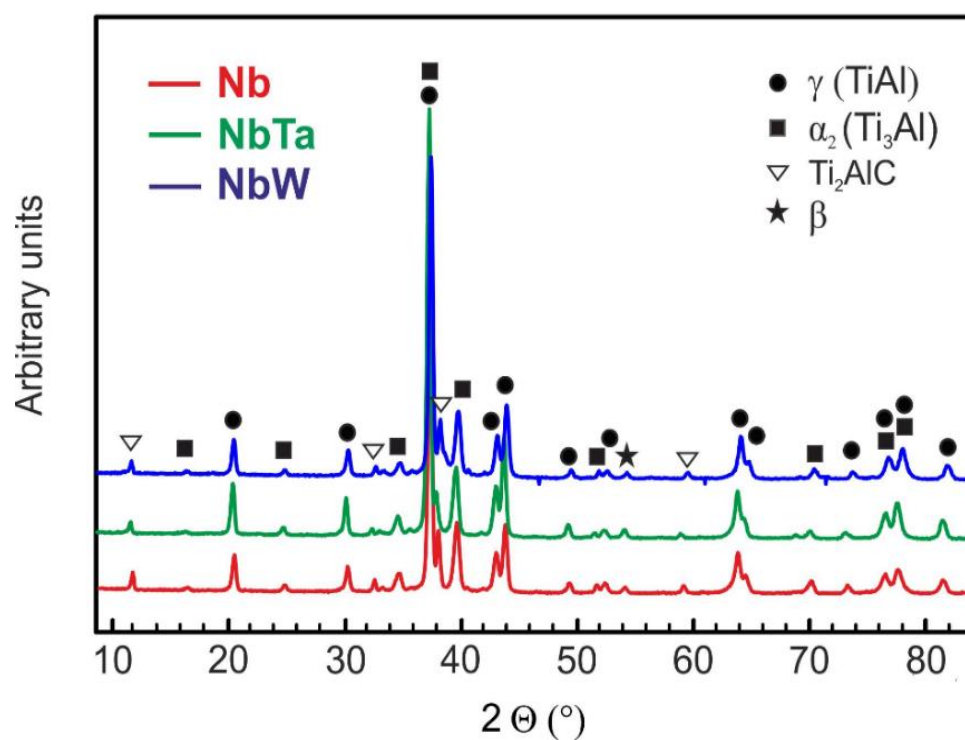


Figure 2. The typical XRD patterns of tilt-cast Nb, NbTa, and NbW alloys.

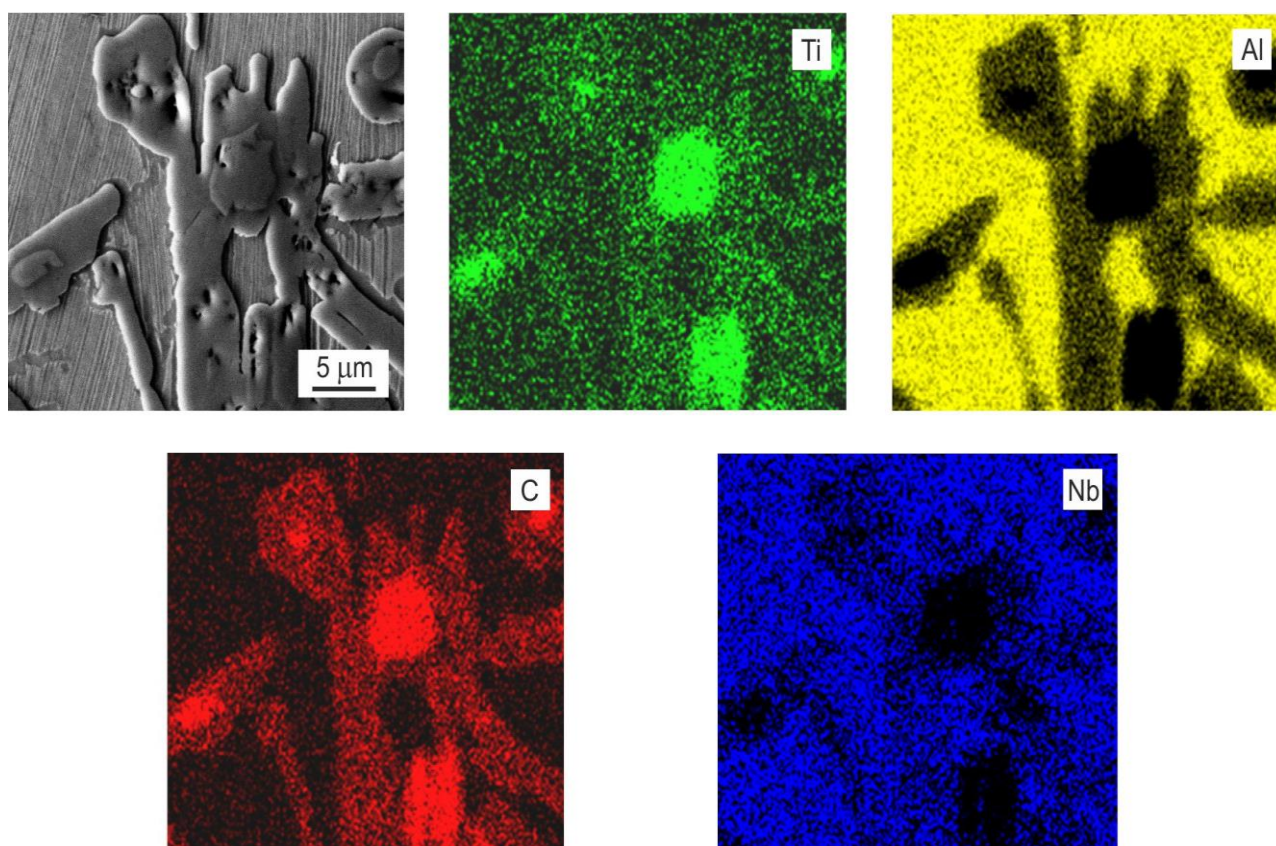


Figure 3. SEM micrograph and corresponding EDS map analysis of the tilt-cast Nb alloy.

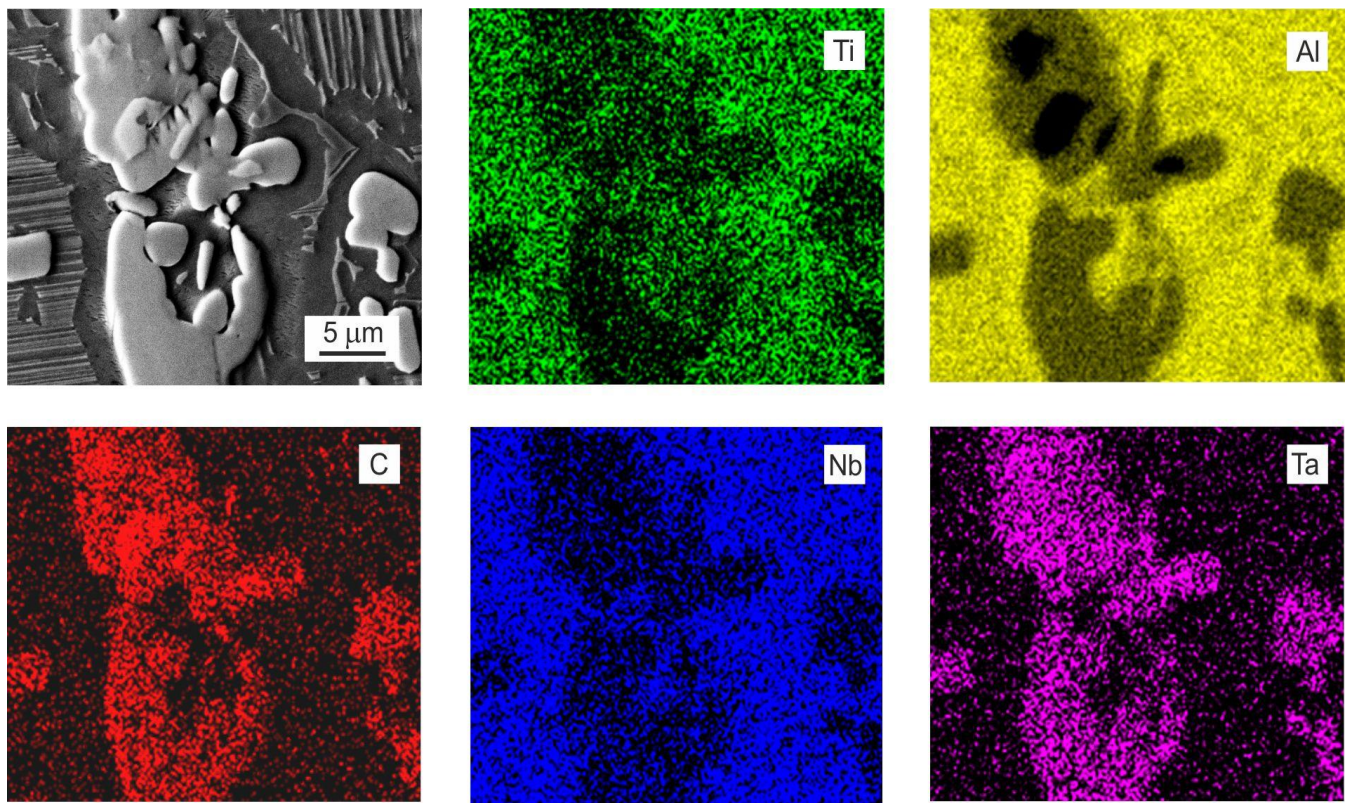


Figure 4. SEM micrograph and corresponding EDS map analysis of the tilt-cast NbTa alloy.

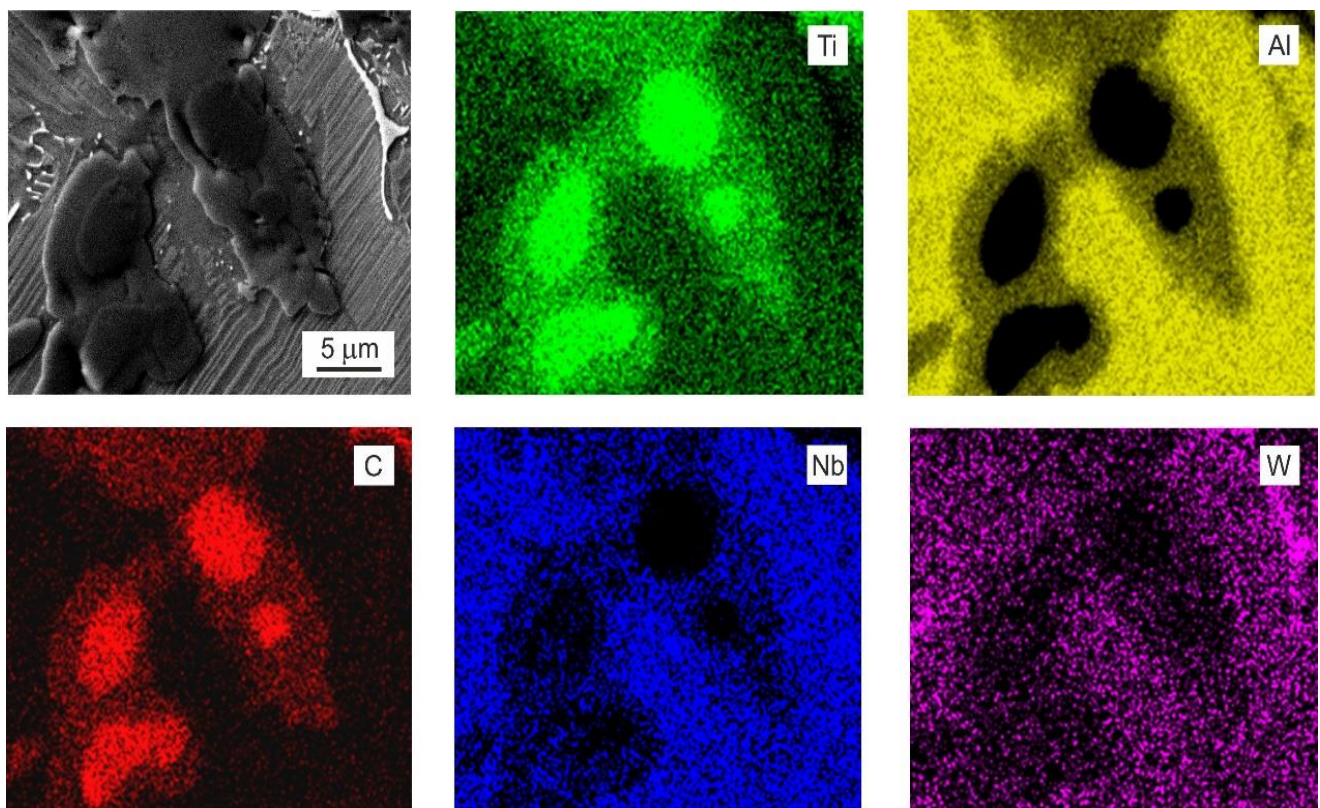


Figure 5. SEM micrograph and corresponding EDS map analysis of the tilt-cast NbW alloy.

The results of the statistical evaluation of quantitative image analysis data of carbide particles, such as mean length of major axis L_{maj} , mean length minor axis L_{min} , volume fraction V_C , and shape factor defined as $S_F = 4\pi A/P^2$, where A is the area and P is the perimeter of the carbide particle, are summarised in Table 3. It is clear from Table 3 that the alloying with Ta and W does not statistically affect the volume fraction of the primary carbide particles, which is measured to be about 7.4 vol.% in the studied alloys. The increase in the shape factor S_F in the NbW alloy indicates an increased number of irregularly shaped particles at the expense of a decreasing number of plate-like ones compared to those in the Nb and NbTa alloys. The alloying with Ta and W decreases the size of carbide particles, indicated by a decrease in mean lengths of major and minor axes, as shown in Table 3.

Table 3. Measured microstructural parameters of the tilt-cast Nb, NbTa, and NbW alloys.

Alloy	L_{maj} (μm)	L_{min} (μm)	S_F	V_C (vol.%)	d (μm)	λ (μm)
Nb	13.0 ± 0.4	3.8 ± 0.1	0.36 ± 0.05	7.5 ± 0.4	33.6 ± 0.6	0.638 ± 0.019
NbTa	10.5 ± 0.4	2.3 ± 0.1	0.37 ± 0.05	7.1 ± 0.6	36.6 ± 0.7	0.678 ± 0.014
NbW	11.0 ± 0.3	3.6 ± 0.1	0.43 ± 0.01	7.7 ± 0.5	42.5 ± 0.8	0.531 ± 0.009

The microstructure of the tilt-cast Nb, NbTa, and NbW alloys consists of equiaxed grains with nearly lamellar microstructure, as seen in Figure 1. Figure 6 shows the statistical evolution of the measured grain size (about 1000 measurements for each alloy) and interlamellar spacing (about 2000 measurements for each alloy). The correlation coefficients of the log-normal regression curves of grain size are better than $r^2 = 0.98$, as seen in Figure 6a. The statistical mean values of the grain size d are summarised in Table 3. The measured mean grain size ranging from 33.6 to 42.5 μm indicates that the formation of about 7.4 vol.% of primary carbide particles very efficiently refines the grain structure of the studied alloys compared to that observed in numerous as-cast TiAl-based alloys without or low volume fraction primary carbide particles [46,57,58]. Although there are clear statistical differences between the mean grain size measured in the studied alloys, indicating the more efficient effect of the carbide particles on the nucleation rate and grain growth in the Nb alloy, this effect can be appropriately evaluated only after full heat treatments required for microstructure optimisation [41,44,59].

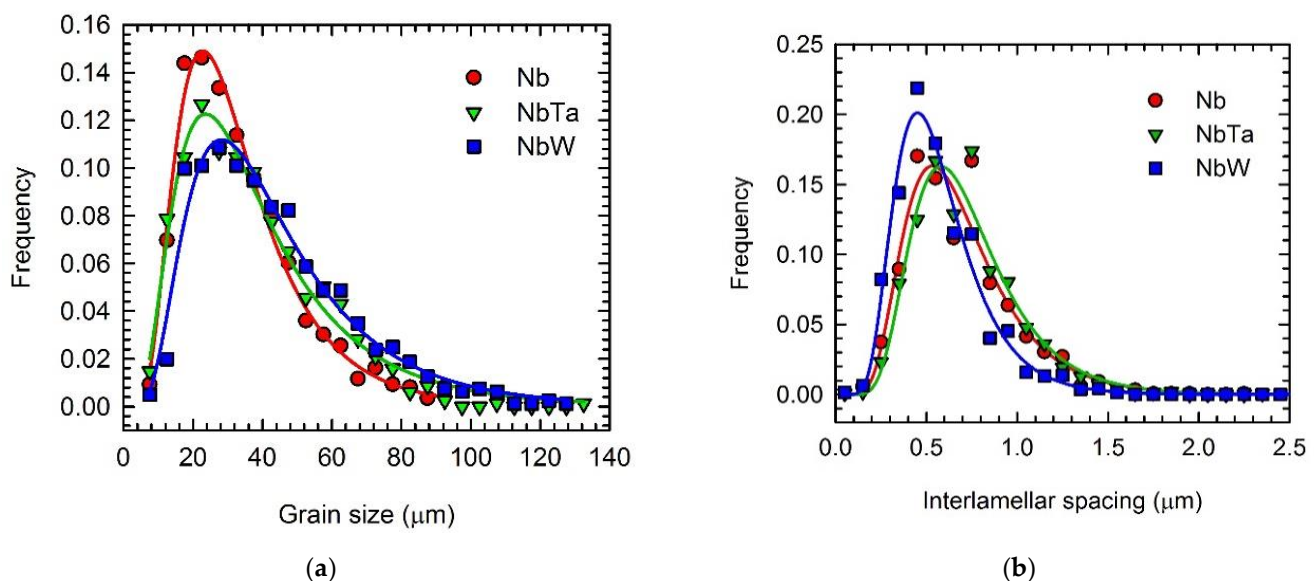


Figure 6. Measured grain size and interlamellar spacing in Nb, NbTa, and NbW alloys after tilt casting: (a) log-normal distribution curves of grain size, (b) log-normal distribution curves of α_2 - α_2 interlamellar spacing. The types of the distribution curves are marked in the figure.

Figure 6b shows log-normal distribution curves of α_2 - α_2 interlamellar spacing λ . It should be noted that the correlation coefficients of the log-normal regression curves are better than $r^2 = 0.97$. It is clear from Table 3 that the alloying with W significantly refines the lamellar microstructure and leads to a significantly lower mean interlamellar spacing λ in the tilt-cast NbW alloy compared to that of the Nb and NbTa ones.

3.3. Nanohardness, Microhardness, and Hardness

Figure 7 shows the effect of Ta and W on Vickers hardness and indentation elastic modulus of Ti-45Al-5.6Nb-2C (at.%) alloy. The alloying with Ta and W has no significant effect on average Vickers hardness HV30 measured on the tilt-cast samples. All variations in the Vickers hardness values fall well into the experimental errors of the measurements, as seen in Figure 7a. Similarly, Ta or W additions have no significant effect on the elastic modulus of the studied alloys. All variations in the measured elastic modulus fall into the experimental error of the measurements, as seen in Figure 7b. It should be noted that the average values are calculated from 30 independent measurements carried out for each alloy. The applied load of 298 N was sufficiently high to deform a representative volume and create the indentations with dimensions covering nine or more equiaxed grains in each alloy. Figure 8 shows nanohardness and elastic modulus of the reinforcing (Ti,Nb,X)2AlC particles. Even though the segregation behaviour of Ta differs significantly from that of W in the studied alloys, the measured nanohardness values and indentation elastic modulus for the (Ti,Nb,X)2AlC phase are lower in the NbTa and NbW alloys than those in the Nb alloy, as seen in Figure 8a,b. Figure 9 shows Vickers microhardness of lamellar $\alpha_2 + \gamma$ regions. The Vickers microhardness HV0.05 of the NbW alloy is higher than that of the Nb and NbTa alloys, as shown in Figure 9a. The Vickers microhardness increases with the decreasing of the measured mean interlamellar α_2 - α_2 spacing, as shown in Figure 9b.

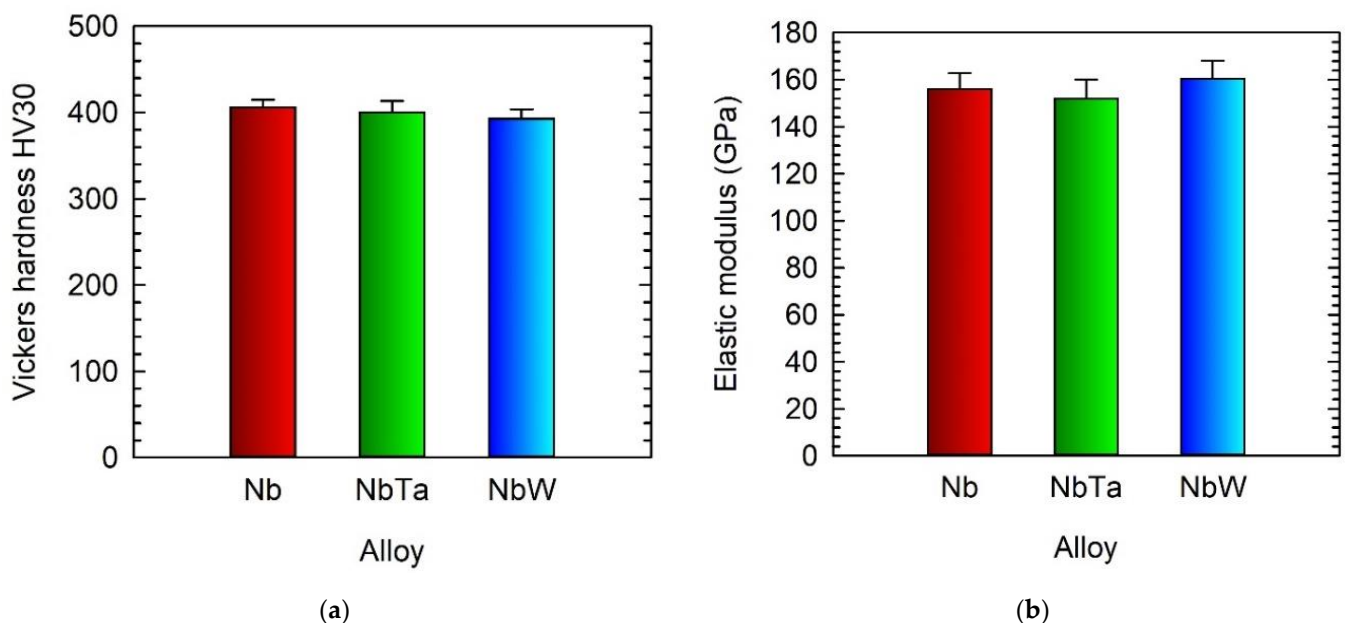


Figure 7. Vickers hardness and elastic modulus of tilt-cast Nb, NbTa, and NbW alloys: (a) Vicker hardness HV30, (b) indentation elastic modulus. The studied alloys are marked in the figures.

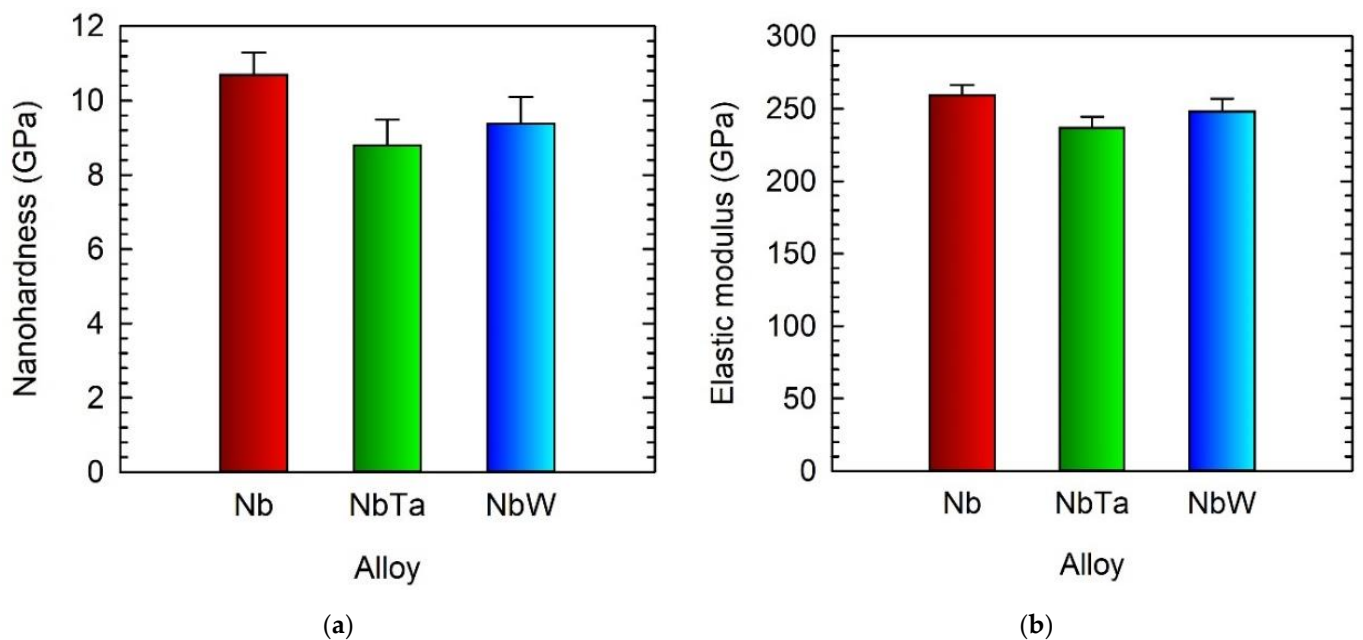


Figure 8. Nanohardness and elastic modulus of Ti_2AlC particles in the tilt-cast Nb, NbTa, and NbW alloys: (a) nanohardness, (b) indentation elastic modulus. The studied alloys are marked in the figures.

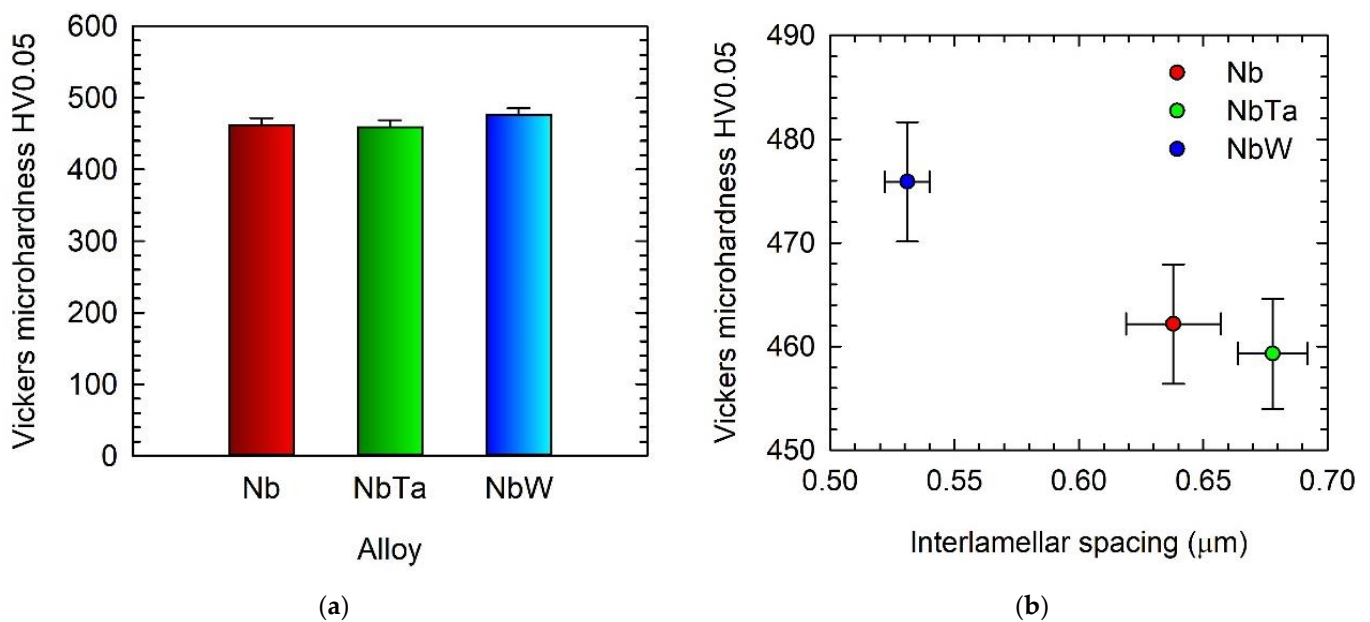


Figure 9. Vickers microhardness of lamellar $\alpha_2 + \gamma$ regions in the tilt-cast Nb, NbTa, and NbW alloys: (a) Vickers microhardness HV0.05, (b) dependence of Vickers microhardness HV0.05 on α_2 - α_2 interlamellar spacing. The studied alloys are marked in the figures.

4. Discussion

4.1. VIM in Graphite Crucibles and Casting into Graphite Moulds

The VIM in graphite crucibles is connected with an increase in carbon content that depends on alloy chemistry, melt temperature, reaction time, quality of graphite, the volume of the melt, and contact area between the melt and graphite crucible [45–47,60]. Szkliniarz and Szkliniarz [43] have reported that the VIM of Ti-47Al-2W-0.5Si (at.%) alloy in graphite crucibles at 1650 °C leads to an increase in C content by 0.35 at.%. Lapin and Klimová [44] have reported an increase in C content by 0.9 at.% in Ti-xAl-8Nb-3.6C-

0.8Mo (at.%) alloys, where $x = 38, 42$ and 45 at.%, during their VIM in graphite crucibles at 1700 °C. The increase in C content can be mainly related to the interactions between carbide forming elements in the melt and graphite walls. Assuming the chemical composition of the studied alloys and Gibbs free energy ΔG of carbide formation at 1650 °C [61], the following exothermic reactions can contribute to the increase in C content in VIM alloys: $\text{Ti} + \text{C} = \text{TiC}$ ($\Delta G = -162$ kJ/mol), $\text{Ta} + \text{C} = \text{TaC}$ and ($\Delta G = -142$ kJ/mol), $\text{Nb} + \text{C} = \text{NbC}$ ($\Delta G = -127$ kJ/mol), $2\text{Nb} + \text{C} = \text{Nb}_2\text{C}$ ($\Delta G = -184$ kJ/mol), and $2\text{W} + \text{C} = \text{W}_2\text{C}$ ($\Delta G = -35$ kJ/mol). The geometrical arrangement of the charge in the graphite crucible and electromagnetic steering of the melt can supply high convective forces for mechanical detachment of carbide particles from the growing reaction layer and their redistribution into the melt. The solid carbide particles can be either preserved, partially dissolved, or fully dissolved in the melt. It should be noted that the extent of the reaction between the graphite crucible and the melt strongly depends on the quality of the graphite crucible. In the case of the studied Nb, NbTa, and NbW alloys, the VIM in high-density isostatic graphite crucibles resulted in a reproducible increase in C content due to graphite–melt interactions by (0.42 ± 0.06) at.% at 1650 °C. In order to achieve the designed chemical composition of the alloys, the content of the alloying TiC particles in the charge was adjusted to this increase in C content resulting from the graphite crucible–melt exothermic reactions.

The studied alloys show a reproducible content of Al. As has been shown in recent works [44,46], the low vacuum pressure of 6.8 Pa (medium vacuum) leads to intensive evaporation of Al during VIM of TiAl-based alloys. Vacuum pressure ranging from 1×10^3 to 1×10^4 Pa (low vacuum) has been reported to be sufficiently high to prevent Al evaporation even in Nb-rich TiAl-based alloys [36,37,43,60].

4.2. Microstructure Formation

Numerous irregularly shaped $(\text{Ti,Nb,X})_2\text{AlC}$ particles contain central regions enriched by C and lean in Al, as shown in Figure 1 and Table 2. However, their size, and especially their chemical composition, differ significantly from a size of 3 μm and chemistry of the pure TiC powder used for the alloying. Hence, during the melting of the charge in graphite crucibles, the TiC powder decomposed, and thermodynamically more stable and chemically more complex nonstoichiometric $(\text{Ti,Nb,X})\text{C}_{1-x}$ particles were formed. In the ternary Ti–Al–C system, the single liquid (L) phase region can be achieved only at temperatures significantly higher than the melt temperature used in the present work. Witusiewicz et al. [62] have calculated that, below full melting of Ti–Al–C alloys, a two-phase region composed of the liquid and nonstoichiometric solid TiC_{1-x} phase is thermodynamically stable. Taking into account the reported thermodynamic calculations and microstructural observations shown in Figures 1 and 3, Figures 4 and 5, the stabilisation temperature of the charge of 1650 °C corresponds to a phase equilibrium $\text{L} + (\text{Ti,Nb,X})\text{C}_{1-x}$ in the studied alloys before casting. After the tilt casting into a cold graphite mould, the temperature of the melt decreases continuously and a new phase equilibrium is achieved according to transformation pathway $\text{L} + (\text{Ti,Nb,X})\text{C}_{1-x} \rightarrow \text{L} + (\text{Ti,Nb,X})_2\text{AlC}$. This reaction/transformation starts by the growth of solid $(\text{Ti,Nb,X})_2\text{AlC}$ layer at the $\text{L}/(\text{Ti,Nb,X})\text{C}_{1-x}$ interface and leads to a partial or full transformation of $(\text{Ti,Nb,X})\text{C}_{1-x}$ particles to the $(\text{Ti,Nb,X})_2\text{AlC}$ phase. Since the remaining liquid is still supersaturated by carbon, the solidification continues by the formation of plate-like $(\text{Ti,Nb,X})_2\text{AlC}$ particles that nucleate spontaneously from the melt, but their growth is restricted by other growing carbide particles. The carbide particles forming in the melt serve as nucleation sites for the formation of β phase, according to transformation pathway $\text{L} + (\text{Ti,Nb,X})_2\text{AlC} \rightarrow \text{L} + \beta + (\text{Ti,Nb,X})_2\text{AlC} \rightarrow \beta + \alpha + (\text{Ti,Nb,X})_2\text{AlC}$. The microstructure formation is finalised by the solid-state phase transformations $\beta + \alpha + (\text{Ti,Nb,X})_2\text{AlC} \rightarrow \beta + \alpha + \gamma + (\text{Ti,Nb,X})_2\text{AlC} \rightarrow \alpha_2 + \gamma + (\text{Ti,Nb,X})_2\text{AlC}$. The presence of γ , β , and $(\text{Ti,Nb,X})\text{C}$ phase regions in the tilt-cast alloys result from Al segregation into the interdendritic region, the incomplete transformation of β to α phase, and insufficient time and temperature for the diffusion-controlled transformation of $(\text{Ti,Nb,X})\text{C}$ to $(\text{Ti,Nb,X})_2\text{AlC}$,

respectively. As shown by Lapin and Klimová [44], the size of the primary carbide particles is strongly affected by the casting technology. Fast turbulent filling of the mould and fast cooling rates lead to the formation of finer primary carbide particles and smaller grain size during centrifugal casting compared to those formed during tilt casting.

4.3. Mechanical Properties

Although the Vickers hardness measurements do not show a clear effect of the alloying on room temperature mechanical properties, the nanohardness and microhardness values indicate some differences between the tilt-cast Nb, NbTa, and NbW alloys. Figure 8 shows the variations in nanohardness values of primary $(\text{Ti,Nb,X})_2\text{AlC}$ particles, indicating softening and lower indentation elastic modulus of the NbTa alloy compared to those in the Nb and NbW alloys. However, this softening cannot be attributed only to the substitution of Ti with Nb and Ta in the $(\text{Ti,Nb,Ta})_2\text{AlC}$ phase when compared with the chemistry of this phase in the Nb and NbW alloys, as seen in Table 2. Meng et al. [63] have shown that a significantly higher concentration of V (atomic radius of V corresponds to that of W) substituting for Ti than the measured variations in Nb, Ta, and W contents in Ti_2AlC phase is required to quantify its solid solution strengthening effect using Vickers hardness measurements. The observed variations in the nanohardness and elastic modulus in the studied alloys can also be significantly affected by the crystallographic orientations of the nanoindentation planes of the $(\text{Ti,Nb,X})_2\text{AlC}$ phase. Liu et al. [64] have calculated that the nanoindentation hardness depends on the nanoindentation crystallographic plane and its increase is also connected with an increase in the elastic modulus. Figure 8 qualitatively shows a very similar evolution of nanohardness with indentation elastic modulus of the $(\text{Ti,Nb,X})_2\text{AlC}$ phase in the Nb, NbTa, and NbW alloys to that calculated by Liu et al. [64] for Ti_2AlC crystals. Despite the statistical number of measurements performed on the carbide particles in each studied alloy (up to 70 measurements), the effect of nanoindentation planes on the variations of the measured nanohardness and indentation elastic modulus values cannot be fully excluded.

The aligned α_2 lamellae are strong barriers to dislocation motion in the lamellar $\alpha_2 + \gamma$ regions. Dislocations generated in the softer γ phase pile-up at α_2/γ interfaces during deformation at room and high temperatures [65,66]. The decrease in the α_2 - α_2 interlamellar spacing in the NbW compared to those of the Nb and NbTa alloys increases the number of strong α_2/γ interfaces that hinder dislocation motion during plastic deformation below the indenter. The increased strain hardening of the lamellar $\alpha_2 + \gamma$ matrix leads to an increase in Vickers microhardness values. As shown by several authors [66,67], the Vickers microhardness can be related to the α_2 - α_2 interlamellar spacing according to a Hall–Petch type relationship in a form $\text{HV} \propto \lambda^{-0.5}$ and also linearly to offset compression yield strength of TiAl-based alloys with lamellar microstructure [68].

5. Conclusions

The effect of Ta and W additions on microstructure and mechanical properties of tilt-cast Ti-45Al-5Nb-2C (at.%) alloy was studied. The following conclusions are reached:

1. The VIM in graphite crucibles followed by tilt casting into graphite moulds leads to the reproducible chemical compositions of the tilt-cast alloys designated as Nb, NbTa, and NbW that correspond well to the nominal ones.
2. The microstructures of the tilt-cast alloys consist of primary plate-like and irregularly shaped $(\text{Ti,Nb,X})_2\text{AlC}$ particles, where X is Ta or W, that are relatively uniformly distributed in the intermetallic matrices composed of α_2 , γ , and $\beta/\text{B2}$ phases. A small amount of $(\text{Ti,Nb,X})\text{C}$ phase is identified in the cores of some coarse irregularly shaped particles.
3. The carbide particles serve as the nucleation sites for β dendrites during solidification and contribute effectively to the grain refinement of the studied tilt-cast Nb, NbTa, and NbW alloys. The alloying with W refines the lamellar $\alpha_2 + \gamma$ microstructure and

leads to the preservation of an untransformed irregularly shaped network of the β /B2 phase during solid-state phase transformations.

4. The alloying with Ta and W has no significant effect on Vickers hardness and indentation elastic modulus of the studied Nb, NbTa, and NbW alloys. The measured nanohardness and indentation modulus of the reinforcing $(\text{Ti,Nb,Ta})_2\text{AlC}$ particles in the Ta containing NbTa alloy are significantly lower compared to those of $(\text{Ti,Nb})_2\text{AlC}$ or $(\text{Ti,Nb,W})_2\text{AlC}$ phases of the Nb and NbW alloys, respectively. The Vickers microhardness of lamellar $\alpha_2 + \gamma$ regions measured in the NbW alloy is significantly higher than that of the Nb and NbTa alloys.

Author Contributions: Conceptualisation, J.L.; methodology, J.L. and K.K.; validation, J.L.; formal analysis, J.L. and K.K.; investigation, K.K. and J.L.; writing—original draft preparation, J.L.; writing—review and editing, J.L. and K.K.; visualisation, K.K. and J.L.; supervision, J.L. All authors have read and agreed to the published version of the manuscript.

Funding: This research was funded by the Slovak Grant Agency for Science under the contract VEGA 2/0074/19 and the Slovak Research and Development Agency under the contracts APVV-20-0505 and APVV-15-0660.

Institutional Review Board Statement: Not applicable.

Informed Consent Statement: Not applicable.

Data Availability Statement: All the data generated during this study are included in this article.

Acknowledgments: The authors would like to thank Soňa Kružílková for technical assistance and metallographic preparation of samples.

Conflicts of Interest: The authors declare no conflict of interest. The funders had no role in the design of the study; in the collection, analyses, or interpretation of data; in the writing of the manuscript; or in the decision to publish the results.

References

1. Appel, F.; Paul, J.D.H.; Oehring, M. *Gamma Titanium Aluminide Alloys: Science and Technology*; Wiley-VCH Verlag & Co. KGaA: Weinheim, Germany, 2011.
2. Clemens, H.; Mayer, S. Intermetallic titanium aluminides in aerospace applications—Processing, microstructure and properties. *Mater. High Temp.* **2016**, *33*, 560–570. [\[CrossRef\]](#)
3. Kim, Y.W.; Kim, S.L. Advances in Gammalloy Materials—Processes—Application Technology: Successes, Dilemmas, and Future. *Jom* **2018**, *70*, 553–560. [\[CrossRef\]](#)
4. Rios, O.; Goyel, S.; Kesler, M.S.; Cupid, D.M.; Seifert, H.J.; Ebrahimi, F. An evaluation of high-temperature phase stability in the Ti-Al-Nb system. *Scr. Mater.* **2009**, *60*, 156–159. [\[CrossRef\]](#)
5. Appel, F.; Clemens, H.; Fischer, F.D. Modeling concepts for intermetallic titanium aluminides. *Prog. Mater. Sci.* **2016**, *81*, 55–124. [\[CrossRef\]](#)
6. Bresler, J.; Neumeier, S.; Ziener, M.; Pyczak, F.; Göken, M. The influence of niobium, tantalum and zirconium on the microstructure and creep strength of fully lamellar γ/α_2 titanium aluminides. *Mater. Sci. Eng. A* **2019**, *744*, 46–53. [\[CrossRef\]](#)
7. Liu, Z.C.; Lin, J.P.; Li, S.J.; Chen, G.L. Effects of Nb and Al on the microstructures and mechanical properties of high Nb containing TiAl base alloys. *Intermetallics* **2002**, *10*, 653–659. [\[CrossRef\]](#)
8. Ding, X.F.; Lin, J.P.; Zhang, L.Q.; Su, Y.Q.; Chen, G.L. Microstructural control of TiAl-Nb alloys by directional solidification. *Acta Mater.* **2012**, *60*, 498–506. [\[CrossRef\]](#)
9. Lin, J.P.; Xu, X.J.; Wang, Y.L.; He, S.F.; Zhang, Y.; Song, X.P.; Chen, G.L. High temperature deformation behaviors of a high Nb containing TiAl alloy. *Intermetallics* **2007**, *15*, 668–674. [\[CrossRef\]](#)
10. Ding, X.; Zhang, L.; He, J.; Zhang, F.; Feng, X.; Nan, H.; Lin, J.; Kim, Y.W. As-cast microstructure characteristics dependent on solidification mode in TiAl-Nb alloys. *J. Alloys Compd.* **2019**, *809*, 151862. [\[CrossRef\]](#)
11. Liu, X.; Lin, Q.; Zhang, W.; Van Horne, C.; Cha, L. Microstructure design and its effect on mechanical properties in gamma titanium aluminides. *Metals* **2021**, *11*, 1644. [\[CrossRef\]](#)
12. Jiang, H.; Zhang, K.; Hao, X.J.; Saage, H.; Wain, N.; Hu, D.; Loretto, M.H.; Wu, X. Nucleation of massive gamma during air cooling of Ti46Al8Ta. *Intermetallics* **2010**, *18*, 938–944. [\[CrossRef\]](#)
13. Lapin, J.; Marek, K. Effect of continuous cooling on solid phase transformations in TiAl-based alloy during Jominy end-quench test. *J. Alloys Compd.* **2018**, *735*, 338–348. [\[CrossRef\]](#)
14. Zhang, K.; Hu, R.; Lei, T.; Yang, J. Refinement of massive γ phase with enhanced properties in a Ta containing γ -TiAl-based alloys. *Scr. Mater.* **2019**, *172*, 113–118. [\[CrossRef\]](#)

15. Zhang, K.; Hu, R.; Wang, X.; Yang, J. Precipitation of two kinds of γ laths in massive γ coexisting with γ lamellae in as-cast Ta-containing TiAl-Nb alloys. *Mater. Lett.* **2016**, *185*, 480–483. [[CrossRef](#)]
16. Vojtěch, D.; Popela, T.; Kubásek, J.; Maixner, J.; Novák, P. Comparison of Nb- and Ta-effectiveness for improvement of the cyclic oxidation resistance of TiAl-based intermetallics. *Intermetallics* **2011**, *19*, 493–501. [[CrossRef](#)]
17. Vojtěch, D.; Popela, T.; Hamáček, J.; Kützendörfer, J. The influence of tantalum on the high temperature characteristics of lamellar gamma+alpha 2 titanium aluminide. *Mater. Sci. Eng. A* **2011**, *528*, 8557–8564. [[CrossRef](#)]
18. Lapin, J.; Pelachová, T.; Dománková, M. Long-term creep behaviour of cast TiAl-Ta alloy. *Intermetallics* **2018**, *95*, 24–32. [[CrossRef](#)]
19. Lapin, J.; Pelachová, T.; Witusiewicz, V.T.; Dobročka, E. Effect of long-term ageing on microstructure stability and lattice parameters of coexisting phases in intermetallic Ti-46Al-8Ta alloy. *Intermetallics* **2011**, *19*, 121–124. [[CrossRef](#)]
20. Beddoes, J.; Seo, D.Y.; Saari, H. Long term creep of TiAl + W + Si with polycrystalline and columnar grain structures. *Scr. Mater.* **2005**, *52*, 745–750. [[CrossRef](#)]
21. Seo, D.Y.; Beddoes, J.; Zhao, L. Primary creep behavior of Ti-48Al-2W as a function of stress and lamellar morphology. *Metall. Mater. Trans. A* **2003**, *34 A*, 2177–2190. [[CrossRef](#)]
22. Beddoes, J.; Seo, D.Y.; Chen, W.R.; Zhao, L. Relationship between tensile and primary creep properties of near γ -TiAl intermetallics. *Intermetallics* **2001**, *9*, 915–922. [[CrossRef](#)]
23. Couret, A.; Monchoux, J.; Caillard, D. On the high creep strength of the W containing IRIS-TiAl alloy at 850 °C. *Acta Mater.* **2019**, *181*, 331–341. [[CrossRef](#)]
24. Lapin, J.; Nazmy, M. Microstructure and creep properties of a cast intermetallic Ti-46Al-2W-0.5Si alloy for gas turbine applications. *Mater. Sci. Eng. A* **2004**, *380*, 298–307. [[CrossRef](#)]
25. Lapin, J. Comparative study of creep of cast Ti-46Al-2W-0.5Si and Ti-45Al-2W-0.6Si-0.7B alloys. *Kov. Mater.* **2006**, *44*, 57–64.
26. Lapin, J. Creep behaviour of a cast TiAl-based alloy for industrial applications. *Intermetallics* **2006**, *14*, 115–122. [[CrossRef](#)]
27. Muñoz-Morris, M.A.; Gil, I.; Morris, D.G. Microstructural stability of γ -based TiAl intermetallics containing β phase. *Intermetallics* **2005**, *13*, 929–936. [[CrossRef](#)]
28. Muñoz-Morris, M.A.; Fernández, I.G.; Morris, D.G. Softening produced by the microstructural instability of the intermetallic alloy Ti-46.5Al-2W-0.5Si. *Scr. Mater.* **2002**, *46*, 617–622. [[CrossRef](#)]
29. Schwaighofer, E.; Rashkova, B.; Clemens, H.; Stark, A.; Mayer, S. Effect of carbon addition on solidification behavior, phase evolution and creep properties of an intermetallic β -stabilized γ -TiAl based alloy. *Intermetallics* **2014**, *46*, 173–184. [[CrossRef](#)]
30. Song, L.; Hu, X.; Wang, L.; Stark, A.; Lazurenko, D.; Lorenz, U.; Lin, J.; Pyczak, F.; Zhang, T. Microstructure evolution and enhanced creep property of a high Nb containing TiAl alloy with carbon addition. *J. Alloys Compd.* **2019**, *807*, 151649. [[CrossRef](#)]
31. Wang, L.; Oehring, M.; Lorenz, U.; Stark, A.; Pyczak, F. New insights into perovskite-Ti₃AlC precipitate splitting in a Ti-45Al-5Nb-0.75C alloy by transmission electron microscopy. *Intermetallics* **2018**, *100*, 70–76. [[CrossRef](#)]
32. Gabrisch, H.; Stark, A.; Schimansky, F.P.; Wang, L.; Schell, N.; Lorenz, U.; Pyczak, F. Investigation of carbides in Ti-45Al-5Nb-xC alloys ($0 \leq x \leq 1$) by transmission electron microscopy and high energy-XRD. *Intermetallics* **2013**, *33*, 44–53. [[CrossRef](#)]
33. Tian, W.H.; Nemoto, M. Effect of carbon addition on the microstructures and mechanical properties of γ -TiAl alloys. *Intermetallics* **1997**, *5*, 237–244. [[CrossRef](#)]
34. Wang, L.; Zenk, C.; Stark, A.; Felfer, P.; Gabrisch, H.; Göken, M.; Lorenz, U.; Pyczak, F. Morphology evolution of Ti₃AlC carbide precipitates in high Nb containing TiAl alloys. *Acta Mater.* **2017**, *137*, 36–44. [[CrossRef](#)]
35. Wang, L.; Gabrisch, H.; Lorenz, U.; Schimansky, F.P.; Schreyer, A.; Stark, A.; Pyczak, F. Nucleation and thermal stability of carbide precipitates in high Nb containing TiAl alloys. *Intermetallics* **2015**, *66*, 111–119. [[CrossRef](#)]
36. Klimová, A.; Lapin, J. The effect of heat treatment on microstructure and hardness of in-situ Ti-38Al-7.5Nb-5C-0.9Mo composite. *Kov. Mater.* **2020**, *58*, 433–443. [[CrossRef](#)]
37. Klimová, A.; Lapin, J. Effect of Al content on microstructure of Ti-Al-Nb-C-Mo composites reinforced with carbide particles. *Kov. Mater.* **2019**, *57*, 377–387. [[CrossRef](#)]
38. Klimová, A.; Lapin, J. Effects of C and N additions on primary MAX phase particles in intermetallic Ti-Al-Nb-Mo matrix in-situ composites prepared by vacuum induction melting. *Kov. Mater.* **2019**, *57*, 151–157. [[CrossRef](#)]
39. Lapin, J.; Štamborská, M.; Pelachová, T.; Bajana, O. Fracture behaviour of cast in-situ TiAl matrix composite reinforced with carbide particles. *Mater. Sci. Eng. A* **2018**, *721*, 1–7. [[CrossRef](#)]
40. Chen, R.; Fang, H.; Chen, X.; Su, Y.; Ding, H.; Guo, J.; Fu, H. Formation of TiC/Ti₂AlC and $\alpha_2 + \gamma$ in in-situ TiAl composites with different solidification paths. *Intermetallics* **2017**, *81*, 9–15. [[CrossRef](#)]
41. Lapin, J.; Klimová, A.; Gabalcová, Z.; Pelachová, T.; Bajana, O.; Štamborská, M. Microstructure and mechanical properties of cast in-situ TiAl matrix composites reinforced with (Ti,Nb)₂AlC particles. *Mater. Des.* **2017**, *133*, 404–415. [[CrossRef](#)]
42. Liu, J.; Zhang, F.; Na, H.; Feng, X.; Ding, X. Effect of C addition on as-cast microstructures of high Nb containing TiAl alloys. *Metals* **2019**, *9*, 1201. [[CrossRef](#)]
43. Szkliniarz, W.; Szkliniarz, A. Microstructure and properties of TiAl-based alloys melted in graphite crucible. *Metals* **2021**, *11*, 669. [[CrossRef](#)]
44. Lapin, J.; Klimová, A. Vacuum induction melting and casting of TiAl-based matrix in-situ composites reinforced by carbide particles using graphite crucibles and moulds. *Vacuum* **2019**, *169*, 108930. [[CrossRef](#)]
45. Szkliniarz, W.; Szkliniarz, A. The characteristics of TiAl-based alloys melted in graphite crucibles. *Mater. Sci. Technol.* **2019**, *35*, 297–305. [[CrossRef](#)]

46. Kamyshnykova, K.; Lapin, J. Vacuum induction melting and solidification of TiAl-based alloy in graphite crucibles. *Vacuum* **2018**, *154*, 218–226. [[CrossRef](#)]
47. Barbosa, J.J.; Ribeiro, C.S. Influence of crucible material on the level of contamination in TiAl using induction melting. *Int. J. Cast Met. Res.* **2000**, *12*, 293–301. [[CrossRef](#)]
48. Čegan, T.; Szurman, I.; Kursá, M.; Holešínský, J.; Vontorová, J. Preparation of TiAl-based alloys by induction melting in graphite crucibles. *Kov. Mater.* **2015**, *53*, 69–78. [[CrossRef](#)]
49. Lapin, J.; Štamborská, M.; Pelachová, T.; Čegan, T.; Volodarskaja, A. Hot deformation behaviour and microstructure evolution of TiAl-based alloy reinforced with carbide particles. *Intermetallics* **2020**, *127*, 106962. [[CrossRef](#)]
50. Lapin, J.; Pelachová, T.; Bajana, O. High temperature deformation behaviour and microstructure of cast in-situ TiAl matrix composite reinforced with carbide particles. *J. Alloys Compd.* **2019**, *797*, 754–765. [[CrossRef](#)]
51. Štamborská, M.; Lapin, J.; Bajana, O. Effect of carbon on the room temperature compressive behaviour of Ti-44.5Al-8Nb-0.8Mo-xC alloys prepared by vacuum induction melting. *Kov. Mater.* **2018**, *56*, 349–356. [[CrossRef](#)]
52. Fang, H.; Chen, R.; Chen, X.; Yang, Y.; Su, Y.; Ding, H.; Guo, J. Effect of Ta element on microstructure formation and mechanical properties of high-Nb TiAl alloys. *Intermetallics* **2019**, *104*, 43–51. [[CrossRef](#)]
53. Zollinger, J.; Lapin, J.; Daloz, D.; Combeau, H. Influence of oxygen on solidification behaviour of cast TiAl-based alloys. *Intermetallics* **2007**, *15*, 1343–1350. [[CrossRef](#)]
54. Huang, A.; Loretto, M.H.; Hu, D.; Liu, K.; Wu, X. The role of oxygen content and cooling rate on transformations in TiAl-based alloys. *Intermetallics* **2006**, *14*, 838–847. [[CrossRef](#)]
55. Lefebvre, W.; Menand, A.; Loiseau, A. Influence of oxygen on phase transformations in a Ti-48 At. pct Al alloy. *Metall. Mater. Trans. A* **2003**, *34*, 2067–2075. [[CrossRef](#)]
56. Wei, Y.; Zhang, Y.; Zhou, H.; Lu, G.; Xu, H. First-principles investigation on shear deformation of a TiAl/Ti₃Al interface and effects of oxygen. *Intermetallics* **2012**, *22*, 41–46. [[CrossRef](#)]
57. Lapin, J.; Kamyshnykova, K. Processing, microstructure and mechanical properties of in-situ Ti₃Al+TiAl matrix composite reinforced with Ti₂AlC particles prepared by centrifugal casting. *Intermetallics* **2018**, *98*, 34–44. [[CrossRef](#)]
58. Kamyshnykova, K.; Lapin, J. Grain refinement of cast peritectic TiAl-based alloy by solid-state phase transformations. *Kov. Mater.* **2018**, *56*, 277–287. [[CrossRef](#)]
59. Lapin, J.; Kamyshnykova, K.; Klimova, A. Comparative study of microstructure and mechanical properties of two TiAl-based alloys reinforced with carbide particles. *Molecules* **2020**, *25*, 3423. [[CrossRef](#)]
60. Szkliniarz, W.; Szkliniarz, A. The chemical composition and microstructure of Ti-47Al-2W-0.5Si alloy melted in ceramic crucibles. *Solid State Phenom.* **2012**, *191*, 211–220. [[CrossRef](#)]
61. Shatynski, S.R. The thermochemistry of transition metal carbides. *Oxid. Met.* **1979**, *13*, 105–118. [[CrossRef](#)]
62. Witusiewicz, V.T.; Hallstedt, B.; Bondar, A.A.; Hecht, U.; Sleptsov, S.V.; Velikanova, T.Y. Thermodynamic description of the Al-C-Ti system. *J. Alloys Compd.* **2015**, *623*, 480–496. [[CrossRef](#)]
63. Meng, F.L.; Zhou, Y.C.; Wang, J.Y. Strengthening of Ti₂AlC by substituting Ti with V. *Scr. Mater.* **2005**, *53*, 1369–1372. [[CrossRef](#)]
64. Liu, P.; Xie, J.; Wang, A.; Ma, D.; Mao, Z. An interatomic potential for accurately describing the atomic-scale deformation behaviors of Ti₂AlC crystal. *Comput. Mater. Sci.* **2020**, *182*. [[CrossRef](#)]
65. Lapin, J.; Kamyshnykova, K.; Pelachová, T.; Nagy, Š. Effect of carbon addition and cooling rate on lamellar structure of peritectic TiAl-based alloy. *Intermetallics* **2021**, *128*, 107007. [[CrossRef](#)]
66. Appel, F.; Wagner, R. Microstructure and deformation of two-phase γ -titanium aluminides. *Mater. Sci. Eng. R* **1998**, *22*, 187–268. [[CrossRef](#)]
67. Lapin, J. Effect of lamellar structure on microhardness and yield stress of directionally solidified intermetallic Ti-46Al-2W-0.5Si alloy. *J. Mater. Sci. Lett.* **2003**, *22*, 747–749. [[CrossRef](#)]
68. Lapin, J.; Ondruš, L.; Nazmy, M. Directional solidification of intermetallic Ti-46Al-2W-0.5Si alloy in alumina moulds. *Intermetallics* **2002**, *10*, 1019–1031. [[CrossRef](#)]